Electronic Supplementary Information

Direct three-dimensional imaging of polymer-water interfaces by nanoscale hard X-ray phase tomography

Yin Cheng,[a,d] Heikki Suhonen,[b] Lukas Helfen,[*a,b] Junsheng Li,[c,e] Feng Xu,[a] Michael Grunze,[e,f] Pavel A. Levkin,[*c,e] and Tilo Baumbach[a]

[a] *Institute for Photon Science and Synchrotron Radiation (IPS), Karlsruhe Institute of Technology (KIT), D-76344 Karlsruhe, Germany. Tel: +49(0)721608 26288; Fax: +49(0)721608 26287; E-mail: lukas.helfen@kit.edu*
[b] *European Synchrotron Radiation Facility (ESRF), F-38043 Grenoble, France. Tel: +33 47688 2558*
[c] *Institute of Toxicology and Genetics (ITG), Karlsruhe Institute of Technology (KIT), D-76344 Karlsruhe, Germany. Tel: +49 721608 29175; E-mail: pavel.levkin@kit.edu*
[d] *Freiburg Materials Research Center (FMF), University of Freiburg, D-79104 Freiburg, Germany*
[e] *Department of Applied Physical Chemistry, University of Heidelberg, Im Neuenheimer Feld 253, 69120 Heidelberg, Germany*
[f] *Present address: Institute of Functional Interfaces, Karlsruhe Institute of Technology, 76344 Eggenstein-Leopoldshafen, Germany*

In the current Electronic Supplementary Information (ESI), the following main aspects will be covered:

- A schemetic drawing shows the preparation of slippery BMA-EDMA surface.
- An overview of the hard X-ray phase contrast imaging is introduced, including most of the principal references. Specifically, the propagation-based X-ray phase contrast imaging technique which has been employed in the present paper is discussed.
- A detailed imaging experiment protocol is depicted.
- The maximum radiation dose delivery to the sample that under investigation is estimated.
- The rest results of slippery BMA-EDMA surface (sample #5 – #9) are presented. The direct tomographic reconstructions without phase retrieval are included as well as their comparisons to the phase retrieved reconstructions.
- A concise yet comprehensive perspective is enclosed. Two potential surface or interface investigations that can use *in situ* X-ray phase contrast nano-imaging are given. New

opportunities that emerge from the further development of X-ray phase nanotomography are addressed.

1 Preparation of slippery surface using microporous BMA-EDMA surface

Figure S1 illustrates a scheme of the preparation process of slippery BMA-EDMA surface using the porous BMA-EDMA surface, as described in Section 2.1 in the main article.

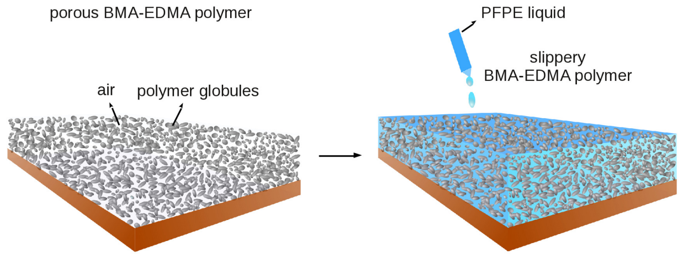

Fig. S1 A representation of the fabrication of the slippery BMA-EDMA surface by infusion of the porous polymer with a perfluoropolyether fluid.

2 Hard X-ray phase contrast imaging

When a wavefront of spatially coherent hard X-rays penetrates an object, it undergoes not only attenuation but also a phase shift. This interaction can be expressed by the complex refractive index of the object: $n = 1 - \delta + i\beta$. The imaginary part β determines the X-ray absorption by the object and is proportional to the material linear attenuation coefficient $\mu = 4\pi\beta/\lambda$ (where λ is the X-ray wavelength). The amplitude modulation of the wave is described by $A(x,y) = \frac{2\pi}{\lambda}\int\beta(x,y,z)\,\mathrm{d}z$, where z is the wave propagation direction. Due to different attenuation properties of materials, the image contrast is generated by different intensity loss right behind the object. This well-known absorption contrast has been commonly used in traditional X-ray imaging. In contrast, the real part decrement of the refractive index δ only causes the distortion of X-ray wavefront and results in the change of the wave phase. And the phase shift induced by the object can be written as $\phi(x,y) = -\frac{2\pi}{\lambda}\int\delta(x,y,z)\,\mathrm{d}z$. The contrast that formed by the evolution of the X-ray phase shift is called “phase contrast”.

It is well known that the X-ray absorption contrast works very well for high-Z elements but may produce poor contrast when imaging of light materials. Typically in the hard X-ray region ($\lambda \simeq$1 - 0.1Å), δ is orders of magnitude of 10^3 higher than β for materials consisting of low-Z elements.[1] Therefore, X-ray phase contrast imaging is prior to absorption imaging at least in our current application – imaging of polymer and liquid, which are weak-absorbing materials. On the other hand, phase contrast imaging allows the possibilities to reduce the dose without losing any contrast by going to higher X-ray energies ($\delta \propto E^{-2}$, whereas $\beta \propto E^{-4}$).[2]

Presently, there are several phase contrast methods have been explored or developed mainly including the prorogation-based imaging (PBI),[3–8] the analyzer-based imaging (ABI),[9–11] the grating interferometric (GI) methods[12–15] and so on. In our present imaging experiment, we explored the PBI method on visualization of our polymer surfaces due to the simple experimental geometry and the advantage of highly coherent X-ray source.

In the PBI method, the detector is placed not immediately behind the object but at some certain distances to allow the transmitted X-ray wavefront continues to propagate. This will permit the phase distortion introduced by the object interferes during propagation and develops into intensity modulations. The intensity modulations are then detectable in the image plan and known as the Fresnel diffraction patterns (near-field diffraction) (Figure 1(a)).[16] Between the object and detector, no additional X-ray optical element is needed in PBI. This makes the PBI geometry rather simple compared to others.

The acquired Fresnel patterns contains the phase information of the object and can be approximated as the Laplacian of the wavefront phase profile, $\nabla^2_{xy}\phi(x,y)$.[17] Direct tomographic reconstruction from these patterns without any treatment yields the 3D distribution of the Laplacian of the decrement of refractive index, $\nabla^2_{xyz}\delta(x,y,z)$ – hence, only edges or interfaces will exhibit strong contrast but there is no direct correlation between the reconstructed gray level and material density (Figure S4).

However, if an inverse problem so-called "phase retrieval" is applied to these Fresnel intensity patterns, the phase distortion in the object plane can be retrieved as the phase map (Figure 1(b)) – Each point in the phase map corresponds to the phase shift $\phi(x,y)$ at the object exist plane. Therefore, tomographic reconstruction from these retrieved phase map will result in the 3D distribution of $\delta(x,y,z)$ in the object, being proportional to the local mass density $\delta \approx 1.36\times10^{-6}\rho[\text{g/cm}^3]\lambda^2[\text{Å}]$.[18] An area contrast will be obtained rather than edge-enhancing contrast.

There exist various phase retrieval algorithms for the PBI. Two of them were used in our experiment and depicted in the main article Section 2.2.2.

3 Experiment

3.1 Experimental setup

Nanotomographic scans were performed at the nanoimaging beamline ID22 at the European Synchrotron Radiation Facility (ESRF), Grenoble, France. The beamline layout, optical axis and tomographic geometry are illustrated in Figure S2. In the image, the X-ray radiation comes from the left-side. The X-ray beam is first focused by a pair of KB mirror and then impinges on the specimen which is mounted on a tomographic rotary stage. The transmitted beam continues propagating a certain distance and finally reaches the detector (which is out of the current view).

3.2 Sample geometries

Samples #1 - #5 (Table 1) were kept into cylindrical tubes and filled with distilled water (Figure S3(a)). The tube is made of Polypropylene (PP) (Ø 8 mm, 1 ml (Height $\sim$ 40 mm) Rotilabo®-sample vials H302.1) with tightly fitting caps made of Polyethylene (PE).

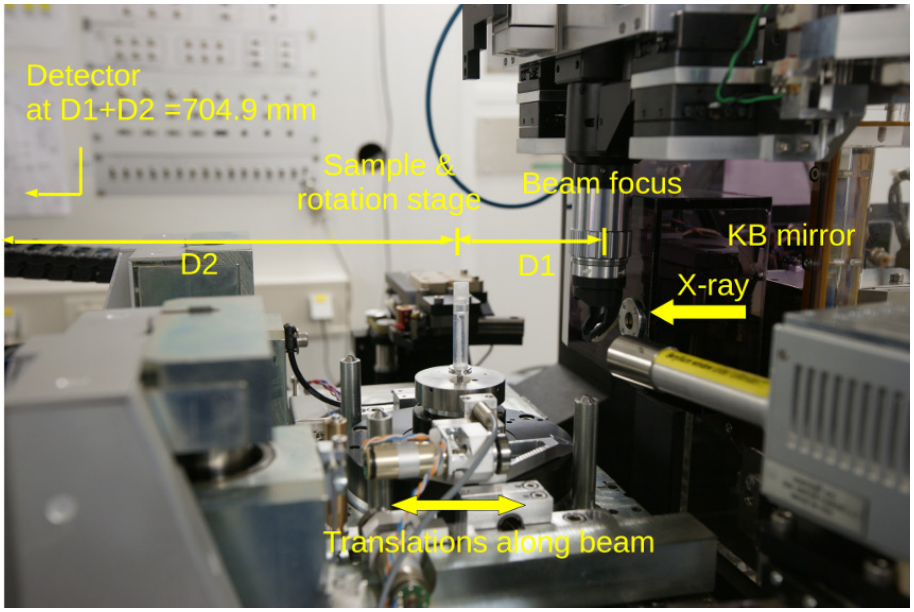

Fig. S2 Photograph of the experimental setup at the nanoimaging endstation ID22NI, ESRF.

Samples #6 - #9 were imaged without sample environment (exposed to air). They were directly fixed onto an aluminum holder which can be further mounted to the tomography rotary stage (Figure S3(b)).

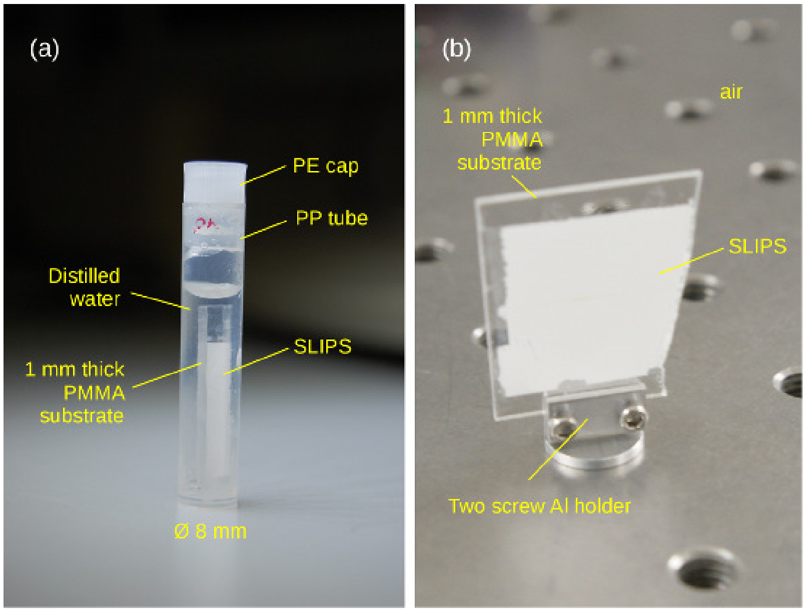

Fig. S3 (a) Photograph of a sample in water environment. It was kept in a sealed PP container that filled with distilled water. The sample surface was placed close to the center of the tube. The sample size is about 5 mm (Width) × 25 mm (Length) × 1 mm (Thickness). (b) Photograph of the scanning geometry of a sample in air environment.

3.3 Radiation dose estimation

X-ray irradiation can sometimes cause sample damages (i.e. structural change, evaporation) if the radiation dose is too high. Therefore, a destructive test was performed during our experiments by varying the exposure time while keeping the number of projections constant. 0.5 s exposure time for each projection was found to be the critical upper limit for causing serious damage to the polymer matrix. Finally, the optimum exposure time was chosen to be 0.2 s by balancing the image quality (SNR) with the radiation dose.

The radiation dose or so-called the absorbed dose is a measure of the energy deposited to a material per unit mass. It is measured as Joules per kilogram and represented by Gy (SI unit). 1 Gy = 1 J/kg.

The dose is directly reflected as the attenuation of the incoming X-ray intensity while passing through the specimen. It obeys the well known Beer-Lambert law as:

$$I = I_0 \mathrm{e}^{-\mu l} \tag{1}$$

where I_0 is the incident beam intensity, I is the transmitted beam intensity, μ is the *linear attenuation coefficient* and l is the sample thickness.

The required experimental parameters for the X-ray dose calculation are listed in Table S1. μ_w, μ_{ens} are the linear attenuation coefficient for water and the linear energy-absorption coefficient for BMA-EDMA surface at the X-ray energy of $E = 29.6$ keV, respectively. These values are taken from the standard DABAX database.[19] The X-ray beam cross section at the sample position was $A = 100 \times 100\ \mu\mathrm{m}^2$ during our experiment.

Table S1 Experimental parameters that are required for the dose calculation.

X-ray energy, E	29.6 keV ($\approx 4.7 \times 10^{-15}$ J)
X-ray flux at sample position, I_0	5.0×10^{11} photons/s
Water (H_2O)	$\mu_w = 0.329$ cm^{-1}, $l_w = 5$ mm
BMA-EDMA	$\mu_{ens} = 0.09$ cm^{-1}, $l_s = 50\mu$m

The X-ray intensity is first attenuated by the surrounding water environment before touching the sample:

$$I_1 = I_0 \mathrm{e}^{-\mu_w l_w} \tag{2}$$

while X-rays continue traversing the sample, the absorbed fraction by the sample is:

$$\eta = 1 - \mathrm{e}^{-\mu_{ens} l_s} \tag{3}$$

the mass of the sample's volume of interest (VOI) that under X-ray illumination is:

$$m_s = \rho_s A l_s \tag{4}$$

$\rho_s = 1.09$ g/cm^3 is the density of BMA-EDMA material (Table 2). Thus, the dose imposed to the sample for every projection is:

$$Dproj = I_1 \eta E \tau / m_s \tag{5}$$

$\tau = 0.2$ s is the exposure time per projection. Substitute all values into Eq. 5, we obtain the dose for each projection is about 330 Gy.

Since 1199 projections were used, the total dose is then estimated to be around 3.8×10^5 Gy for 320 nm low pixel resolution scan, and 1.6×10^6 Gy for 50 nm or 100 nm high pixel resolution scan, respectively. Compared to Langer *et al.*,[20] who applied nanotomography to resolve the human bone ultrastructure, their delivered dose was 8×10^7 Gy (high resolution scan) which is 1.7 orders of magnitude higher than ours. On the other hand, the polymer structure after irradiation correlates well with our SEM images of the same specimen,[21] which indirectly suggests that no significant change of the polymer morphology was induced by the irradiation. We are certain that the radiation effect on the polymer matrix does not affect our surface characterizations.

4 Results of slippery BMA-EDMA surface in water

Figure S4 shows a direct reconstruction from recorded Fresnel patterns of sample #3 – without phase retrieval calculation (see Section 2). We see most of the strong contrasts were formed only adjacent to interfaces or material edges.

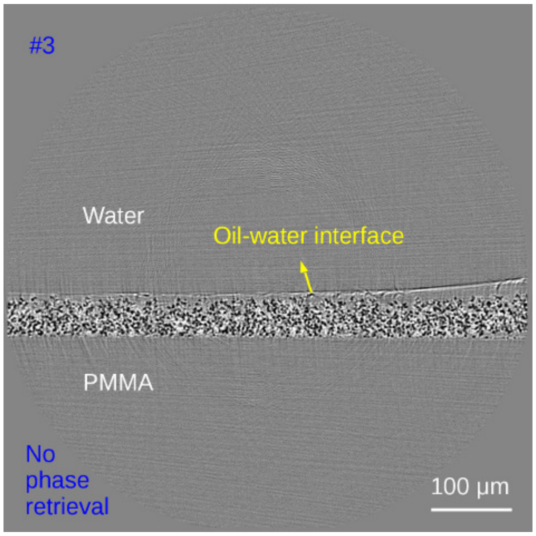

Fig. S4 Direct reconstruction of porous BMA-EDMA surface (sample #3) without phase retrieval. Edge enhancements were observed in the vicinity of structural edges, i.e. at the oil-water interface, at the outer shell of individual polymer globules.

Figure S5 shows a 50 nm high resolution phase reconstructed 2D cross section of slippery BMA-EDMA surface on glass substrate (sample #5). The result is analogous to what we have observed in Figure 5. Reconstruction artifacts due to strong phase variation were also observed here at the interface between water and the lubricant layer. The image quality was also affected by the high-absorbing glass substrate.

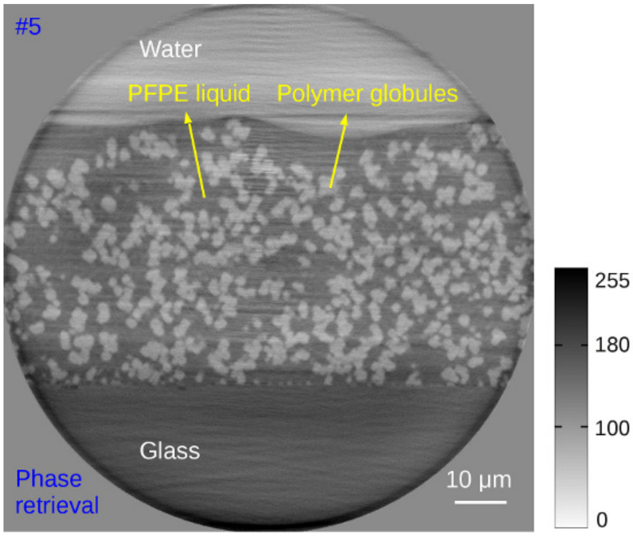

Fig. S5 Phase reconstruction of slippery BMA-EDMA surface on glass substrate (sample #5). Pixel size 50 nm.

5 Results of slippery BMA-EDMA surface in air

Reconstructed 2D sections of SLIPS on the PMMA substrates (sample #6, #7), and on the glass substrates (sample #8, #9) are shown in Figure S6 - S7 and Figure S8 - S9, respectively. In these figures, one notes that the phase reconstructions (a) correctly reproduce the local mass density of different materials, while the direct reconstructions (b) only reflect the high sensitivity to the material boundaries (see Section 2).

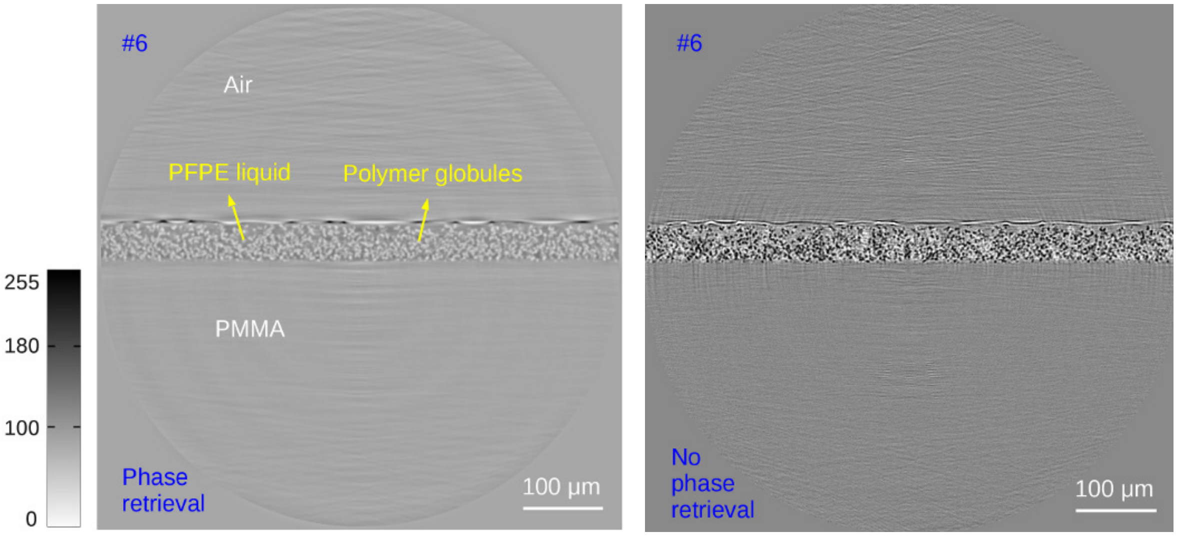

(a) Phase reconstruction.

(b) Direct reconstruction without phase retrieval exhibits only strong edge enhancement.

Fig. S6 Sample #6: Comparison of reconstructions from phase retrieval (a) and non phase retrieval (b). Pixel size 320 nm.

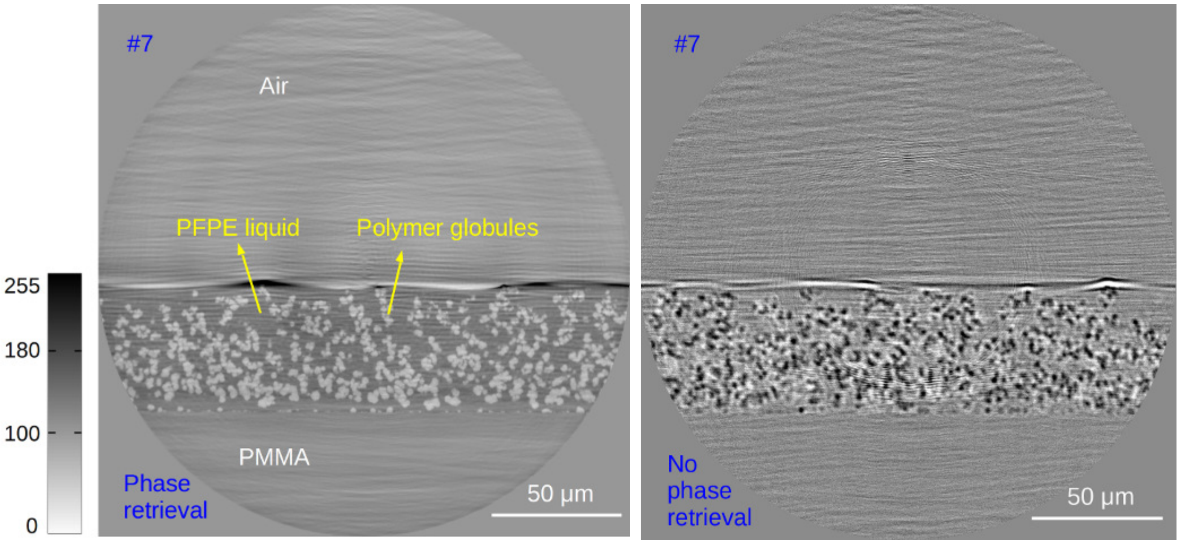

(a) Phase reconstruction.

(b) Edge enhancement is seen from direct reconstruction of recorded radiographs – without phase retrieval.

Fig. S7 Sample #7: Comparison of reconstructions from phase retrieval (a) and non phase retrieval (b). Pixel size 100 nm.

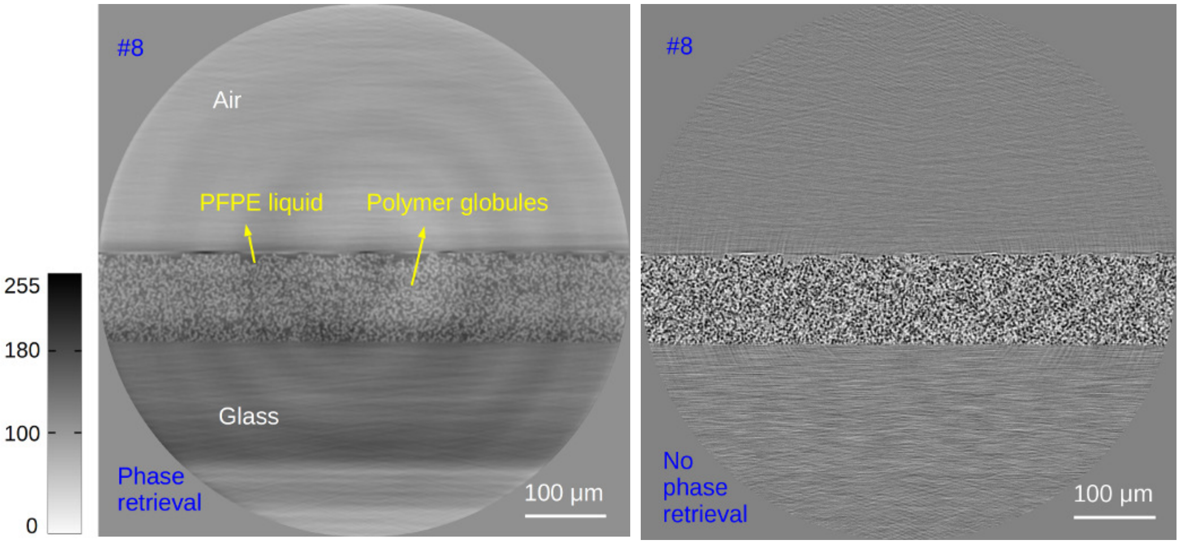

(a) Phase reconstruction.

(b) Edge enhancement is seen from direct reconstruction of recorded radiographs – without phase retrieval.

Fig. S8 Sample #8: Comparison of reconstructions from phase retrieval (a) and non phase retrieval (b). Pixel size 320 nm. Note the BMA-EDMA polymer here has been fabricated to be 100 μm thick.

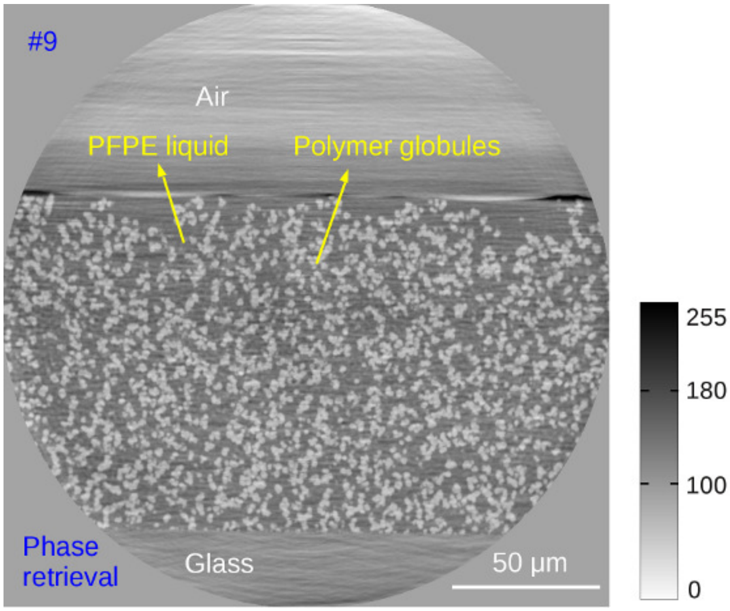

Fig. S9 Phase reconstruction of Sample #9. Pixel size 100 nm. Note the BMA-EDMA polymer here has been fabricated to be 100 μm thick.

6 Perspectives

We have shown the power of X-ray phase tomography for direct 3D imaging of the bulk polymer matrix as well as the buried interfaces between water and these hydrophobic surfaces. The method illustrated here overcomes some of the limitations of many other alternative imaging techniques. In order to keep the slippery surface stable and reduce the phase variation, a 0.8 cm thick water environment has been employed. In this case only hard X-rays can penetrate the specimen. To the best of the authors knowledge it is also the first time that X-ray phase nanotomography has been applied to investigate specimens kept in full water environment. Although our 50 nm achievable pixel resolution may be lower compared to the widely used SEM, the proposed method is not restricted to only superficial imaging and it inherently produces three-dimensional information. This advantage gives a deep insight into the structural relationships within individual phases (solid, liquid and gas) as well as amongst those phases.

For further studies, we believe that the quantitative wetting properties at the submicron scale of the micro- or nano-structured (super)hydrophobic surfaces can be assessed by such direct 3D imaging. Moreover, many other interesting *in situ* avenues of investigations can be undertaken by *time-resolved* X-ray nano-imaging (i.e. the so-called four-dimensional (4D) X-ray cinematography). For instance, visualization of the porous structure formation at various stages of polymerization may help to understand some critical aspects of air trapping properties of these special wettable surfaces.

From the methodological point of view, in the near future, anticipating an even smaller two-dimensional X-ray focal spot size down to 20 nm, higher spatial resolutions will be attainable by phase contrast nanotomography.[22] Lower dose deposition by enabling faster acquisition time and cryo-environment could be foreseen. Finally, recent developments on phase retrieval would also provide more robust algorithms with less restrictions (i.e. extending to multi-materials, strongly absorbing objects, heterogeneous composition with *a priori* knowledge) and accordingly enhance the reconstruction quality.[23–25]

References

1 A. Momose, *Japanese Journal of Applied Physics*, 2005, **44**, 6355–6367.

2 R. Fitzgerald, *Physics Today*, 2000, **53**, 23–26.

3 A. Snigirev, I. Snigireva, V. Kohn, S. Kuznetsov and I. Schelokov, *Review of Scientific Instruments*, 1995, **66**, 5486–5492.

4 P. Cloetens, R. Barrett, J. Baruchel, J.-P. Guigay and M. Schlenker, *Journal of Physics D: Applied Physics*, 1996, **29**, 133.

5 K. A. Nugent, T. E. Gureyev, D. F. Cookson, D. Paganin and Z. Barnea, *Phys. Rev. Lett.*, 1996, **77**, 2961–2964.

6 S. W. Wilkins, T. E. Gureyev, D. Gao, A. Pogany and A. W. Stevenson, *Nature*, 1996, **384**, 335–338.

7 P. Cloetens, W. Ludwig, J. Baruchel, D. van Dyck, J. van Landuyt, J. Guigay and M. Schlenker, *Appl. Phys. Lett.*, 1999, **75**, 2912.

8 P. Cloetens, W. Ludwig, J. Baruchel, J.-P. Guigay, P. Pernot-Rejmánková, M. Salomé-Pateyron, M. Schlenker, J.-Y. Buffière, E. Maire and G. Peix, *Journal of Physics D: Applied Physics*, 1999, **32**, A145.

9 T. J. Davis, D. Gao, T. E. Gureyev, A. W. Stevenson and S. W. Wilkins, *Nature*, 1995, **373**, 595–598.

10 T. J. Davis, T. E. Gureyev, D. Gao, A. W. Stevenson and S. W. Wilkins, *Phys. Rev. Lett.*, 1995, **74**, 3173–3176.

11 D. Chapman, W. Thomlinson, R. E. Johnston, D. Washburn, E. Pisano, N. Gmr, Z. Zhong, R. Menk, F. Arfelli and D. Sayers, *Physics in Medicine and Biology*, 1997, **42**, 2015.

12 A. Momose, *Nuclear Instruments and Methods in Physics Research Section A: Accelerators, Spectrometers, Detectors and Associated Equipment*, 1995, **352**, 622 – 628.

13 A. Momose, T. Takeda, Y. Itai and K. Hirano, *Nature medicine*, 1996, **2**, 473–475.

14 T. Weitkamp, A. Diaz, C. David, F. Pfeiffer, M. Stampanoni, P. Cloetens and E. Ziegler, *Opt. Express*, 2005, **13**, 6296–6304.

15 F. Pfeiffer, T. Weitkamp, O. Bunk and C. David, *Nat Phys*, 2006, **2**, 258–261.

16 P. Cloetens, *Ph.D. thesis*, Vrije Universiteit Brussel and ESRF, 1999.

17 H. Bremmer, *Physica*, 1952, **18**, 469 – 485.

18 A. Guinier, *X-ray diffraction: in crystals, imperfect crystals, and amorphous bodies*, Dover Publications, Mineola, N.Y., 1994.

19 M. Sanchez del Rio and R. J. Dejus, *Proc. SPIE 3448, Crystal and Multilayer Optics*, 1998, 340–345.

20 M. Langer, A. Pacureanu, H. Suhonen, Q. Grimal, P. Cloetens and F. Peyrin, *PLoS ONE*, 2012, **7**, e35691.

21 J. Li, T. Kleintschek, A. Rieder, Y. Cheng, T. Baumbach, U. Obst, T. Schwartz and P. A. Levkin, *ACS Applied Materials & Interfaces*, 2013, **5**, 6704–6711.

22 European Synchrotron Radiation Facility (ESRF) upgrade beamline portfolio, *UPBL4 - Nano-imaging and nano-analysis*, 2011, http://www.esrf.eu/UsersAndScience/Experiments/Imaging/beamline-portfolio.

23 J. P. Guigay, M. Langer, R. Boistel and P. Cloetens, *Opt. Lett.*, 2007, **32**, 1617–1619.

24 M. Langer, P. Cloetens and F. Peyrin, *Image Processing, IEEE Transactions on*, 2010, **19**, 2428–2436.

25 M. Langer, P. Cloetens, A. Pacureanu and F. Peyrin, *Opt. Lett.*, 2012, **37**, 2151–2153.